AIAA JOURNAL
Vol. 54, No. 9, September 2016

Flight-Test Measurement of the Aero-Optical Environment of a Helicopter in Hover

Alice M. Nightingale,* R. Mark Rennie,† Stanislav Gordeyev,† Ryan Kelly,‡ David Cavalieri,§ and Eric J. Jumper¶
University of Notre Dame, Notre Dame, Indiana 46545

DOI: 10.2514/1.J054549

Methods and results are described for flight-test measurements of the aero-optical effect of the near-field flow surrounding a medium-sized helicopter in hover. The data were acquired using a novel, passive measurement approach in which optical wave-front aberrations were computed from the displacements of light-emitting diodes attached to a target array mounted under the helicopter fuselage. The resulting aero-optical data are shown through the rotor downwash and through the engine exhaust of the helicopter, and they are compared to estimates computed using parametric models for the helicopter wake structure and rotor–vortex diffusion. The experimental data provide additional information on the magnitude and frequency content of the aero-optical aberrations, as well as vibration data, that will be valuable for future beam-control and modeling studies.

Nomenclature

A	=	area
a	=	speed of sound
D_{AP}	=	measurement aperture diameter
D_L	=	camera aperture diameter
D_t	=	optical target diameter
$D_{t,\mathrm{CCD}}$	=	light-emitting diode image diameter on camera sensor
d_s	=	size of spatial-averaging region
f	=	frequency
f_L	=	camera focal length
f^*	=	nondimensional frequency, equal to $f/$ blade-passing frequency
I	=	irradiance
I_p	=	pixel intensity
K_{GD}	=	Gladstone–Dale constant
L_1	=	distance from light-emitting diodes to aero-optical flow
L_2	=	distance from aero-optical flow to camera
n	=	index of refraction
R	=	rotor blade radius
r	=	radial coordinate
r_A	=	Airy disk first zero
r_c	=	vortex core radius
St	=	Strehl ratio
$\boldsymbol{s}$	=	wave-front slopes
T	=	solid-body translations
t	=	time
t_S	=	camera shutter time
t^*	=	nondimensional time, equal to t x blade-passing frequency
V_C	=	vortex convection speed
$\boldsymbol{x}$	=	two-dimensional light-emitting diode coordinates in images
$\boldsymbol{x}_p$	=	pixel coordinates
$\boldsymbol{x}_{\mathrm{ref}}$	=	reference locations of light-emitting diodes in images
Γ	=	circulation
θ	=	refraction angle
λ	=	wavelength
ρ	=	density
Ω	=	solid-body rotations

Received 11 June 2015; revision received 12 January 2016; accepted for publication 15 April 2016; published online 12 July 2016.

*Research Assistant Professor, Department of Mechanical and Aerospace Engineering, Hessert Laboratory for Aerospace Research. Member AIAA.

†Research Associate Professor, Department of Mechanical and Aerospace Engineering, Hessert Laboratory for Aerospace Research. Senior Member AIAA.

‡Graduate Student, Department of Mechanical and Aerospace Engineering, Hessert Laboratory for Aerospace Research. Student Member AIAA.

§Research Specialist, Department of Mechanical and Aerospace Engineering, Hessert Laboratory for Aerospace Research. Member AIAA.

¶Professor, Department of Aerospace and Mechanical Engineering. Fellow AIAA.

I. Introduction

OPTICAL communication systems and directed-energy systems require highly focused beams on target in order to achieve system performance objectives. For optical systems mounted on aircraft, the system performance can be compromised by local flows that surround the aircraft and become optically active at compressible-flow speeds. When an optical beam passes through an optically active flow, its wave front becomes aberrated due to the density and associated index-of-refraction variations within the flow. These aberrations can seriously degrade the far-field irradiance pattern of the optical system, thereby reducing the peak irradiance on target. The study of the optical effect of these kinds of near-field compressible flows is called "aero-optics."

For fixed-wing aircraft travelling at compressible-flow speeds, aero-optical effects arise primarily from compressible turbulent flows such as turbulent boundary-layer and shear-layer flows, or inviscid flows such as shock waves. The aero-optical character of these flows has been studied extensively in wind-tunnel tests [1–5]. Flight-test investigations [6–8] are also underway to characterize the aero-optical environment around turret designs that will most likely be employed.

The aero-optical environment surrounding helicopters has been far less extensively investigated. Since even the fastest helicopters travel at incompressible speeds, the kinds of aero-optical flows that are important for fixed-wing aircraft are generally inconsequential for helicopters. Instead, for helicopters, aero-optical aberrations are expected to originate primarily from the wake and (especially) tip vortices that are shed from the helicopter rotor blades, where flow speeds close to and especially within the cores of the vortices are sufficiently high to produce significant density variations and associated optical aberrations [9,10]. As shown by the analyses described in [11], high-speed flows in the tip-vortex cores persist for some distance along the trajectory of the vortex, so that compressible-flow effects can be expected even after the vortices have been convected by the rotor downwash into the line of sight of an optical system mounted within or under the helicopter fuselage [12–15].

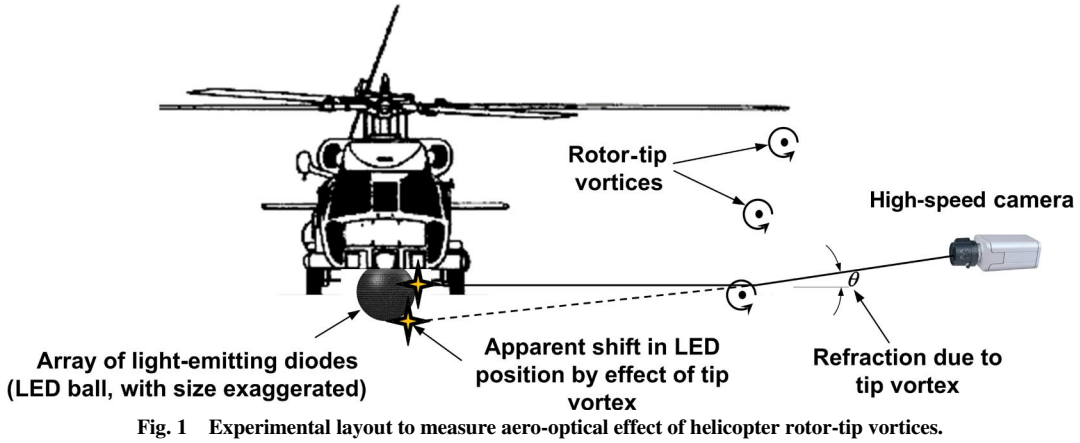

Fig. 1 Experimental layout to measure aero-optical effect of helicopter rotor-tip vortices.

In [12–14], the helicopter rotor wake was computed using prescribed-wake methods [11,16–18] that parametrically defined the location of the rotor-wake vortices without the computational expense of free-vortex methods or full computational fluid dynamics. The aero-optical effect of the rotor wake was then computed using an isentropic approach that was validated against experimental measurements of an isolated tip vortex [15]. Diffusion of the rotor–vortex cores was simulated using empirical correlations [19–21]. These computations showed that the rotor wake generally had a small aero-optical effect on the simulated outgoing beam except for the instants in which a rotor vortex passed through the beam, in which case the far-field Strehl ratio of the outgoing beam could be degraded to less than 0.1 ($\lambda = 1$ μm), depending on atmospheric conditions. Although the simulations described in [12–14] were validated by wind-tunnel measurements of an isolated tip vortex [15], in-flight experimental measurements that would further validate and improve existing models have never, to the knowledge of the authors, been performed before.

This paper describes the experimental measurement and analysis of the aero-optical effect of the rotor wake of a full-scale helicopter in hover. The measurements were performed using a novel, passive approach that allows optical data to be measured through the helicopter rotor wake without the use of complex aiming and tracking instruments and that largely avoids the effects of platform vibrations. The experimental approach is fully described, including measurement methods and results for wave fronts and far-field irradiance patterns of a simulated beam emitted from underneath the helicopter. The flight-test data are compared to the predictions of the prescribed-wake methods described in [12–14].

II. Measurement Approach

The optical aberrations produced by optically active flows are typically evaluated by their effect on an interrogating beam of light with a known initial wave front that passes through the aberrating region of interest. The wave-front distortion can then be measured using instruments like the Shack–Hartman wave-front sensor, in which the beam is first spatially discretized using a lenslet array, and the overall wave front is then constructed from the local wave-front slopes measured at the subapertures. This kind of approach is difficult to implement for helicopter flight tests, however, because the approach requires an interrogating beam and a sensor: one of which is mounted at a measurement station, and the other of which is mounted on the helicopter itself. In this case, tracking and aiming architecture is required to maintain the beam on the sensor, and the helicopter-mounted hardware must be hardened to resist the vibration environment of the helicopter in flight.

To avoid the complications involved in a Shack–Hartman measurement, a simpler, passive measurement approach was adopted for this investigation based conceptually on "synthetic Schlieren" measurements described, for example, in [22]. Specifically, wave-front distortions of the helicopter near-field flow were determined by tracking an array of light-emitting diodes (LEDs) carried by the helicopter using a ground-based high-speed camera. As shown schematically in Fig. 1, the passage of optically aberrating flows between the camera and the LED array produces displacements in the apparent location of the LEDs in the array, which are then measured in postprocessing, used to determine local wave-front slopes, and ultimately used to determine the overall wave-front distortion of the optically aberrating flow. Details of the experimental design of the "synthetic wave-front" approach shown in Fig. 1 are described in the following sections. As will be shown, this approach constitutes a simple yet effective method of acquiring aero-optical data in a flight-test environment.

A. Aero-Optical Effect of Helicopter Tip Vortices

An estimate of the magnitude of the refraction angle θ produced by the helicopter rotor wake can be determined from previous work described in [12–15]. For a helicopter in hover, the circulation of each rotor rolls up rapidly into a tip vortex that forms a helical shape underneath the helicopter and that convects downward. Outside of the cores, the flow around the rotor-tip vortices can be approximated as inviscid and isentropic, so that the large azimuthal velocity component close to the vortex cores produces a local reduction in pressure and density. Refractive-index variations result from the density variations according to the Gladstone–Dale relationship:

$$n(y, z, t) = 1 + K_{\mathrm{GD}}\rho(y, z, t) \tag{1}$$

As shown in [12–15], variations in the streamwise direction x (see Fig. 2) are produced primarily by diffusion of the vortex core; since these variations have a substantially longer length scale than any realistic beam aperture size, these variations in the x direction have been neglected in Eq. (1). For propagation through air at visible and near-IR wavelengths, $K_{\mathrm{GD}} \sim 2.27 \times 10^{-4}$ m^3/kg. The optical path length (OPL) and difference (OPD) of a beam that passes through the vortex are then

$$\mathrm{OPL}(y, t) = \int n(y, z, t)\,\mathrm{d}z \tag{2}$$

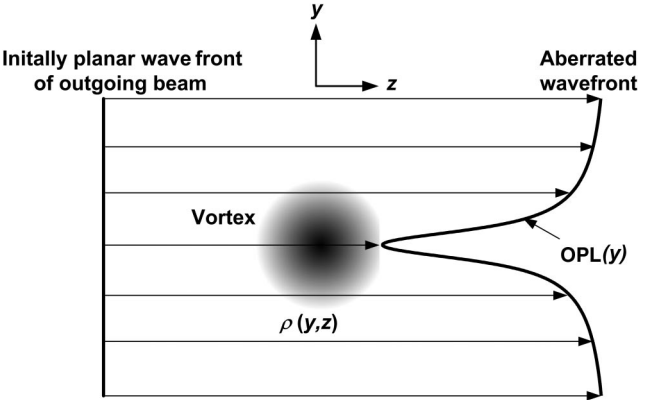

Fig. 2 Schematic of optical aberration due to tip vortex propagating in x direction.

$$\mathrm{OPD}(y,t) = \mathrm{OPL}(y,t) - \overline{\mathrm{OPL}(y,t)} \tag{3}$$

In [15], the aero-optical effect of an isolated aperture-centered tip vortex with a Lamb–Oseen velocity profile was derived for inviscid, isentropic flow, and it was shown to compare closely with experimental measurements. The wave-front distortion of the vortex was shown to scale according to Eq. (4), where the spatial variation of the aberration is contained in the function g:

$$\mathrm{OPD}(y) = K_{\mathrm{GD}}\rho_\infty \frac{\Gamma^2}{a^2 r_c^2} g\left(\frac{y}{r_c}\right) \tag{4}$$

The coordinate system used in Eq. (4) is shown in Fig. 2. Equation (4) shows that the aero-optical effect of the helicopter rotor-tip vortices depends on the rotor circulation Γ and the vortex core radius r_c; the measured OPD (y) also depends on the size of the measurement aperture D_{AP}, which can block part of the vortex aberration if D_{AP} is smaller than the spatial extent of the aberration [15]. Although the circulation Γ of the vortices remains constant after shedding from a rotor, the core radius r_c of each vortex grows due to viscous diffusion as the tip vortices move farther below the helicopter; this means that modeling of the geometry of the rotor wake including a model for the vortex-core diffusion is necessary before an estimate of light refraction angles can be made using Eq. (4).

In [12–15], the geometry of the helical wake below the helicopter was computed using prescribed-wake methods [16,17], which are empirical computational tools consisting of a set of equations that parametrically define the locations of the tip vortices shed from the helicopter rotors; see Fig. 3. Growth of the vortex core with "wake age" (i.e., the total distance along the helical vortex trajectory from the rotor tip to a given point on the vortex) was then modeled using an empirically derived core-growth model [19–21] that included the effects of viscous and turbulent diffusion. In [15], these wake modeling calculations were performed for a generic medium-sized helicopter with $\Gamma = 21\ \mathrm{m}^2/\mathrm{s}$, which is a reasonable value for a medium-sized helicopter in hover [11]. For typical core-growth rates, the calculations gave $r_c \sim 50$ mm at the point that the rotor vortices would pass into the field of regard of an optical system mounted beneath the helicopter.

Using these parameters, the vortex optical effect computed using Eq. (4) is plotted in Fig. 4, which shows that the vortex produces a large depression in OPD near the vortex core that rapidly falls off with distance from the core. For the synthetic wave-front measurements depicted in Fig. 1, the largest refraction angles θ_{MAX} are produced by light rays that pass through the regions with the largest OPD slopes, which occur on either side of the maximum OPD depression at the vortex centerline $y = 0$; for the vortex shown in Fig. 4, $\theta_{\mathrm{MAX}} \sim 15\ \mu$rad. Data provided in [15] also show that the pitch of the helical vortex wake for this case is approximately 2 m. For typical

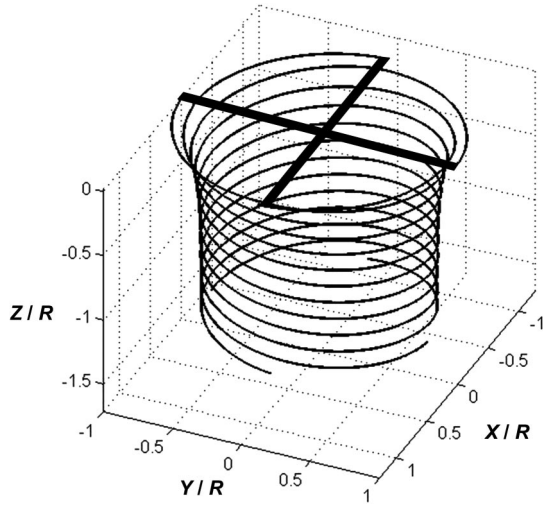

Fig. 3 Example of helical tip-vortex trajectory below a medium-sized helicopter in hover, computed using a prescribed-wake method [12,14].

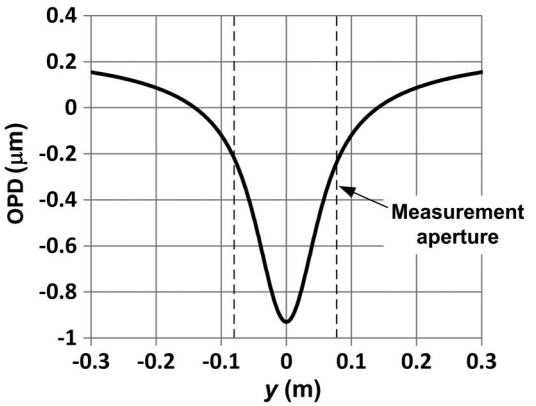

Fig. 4 Optical effect of aperture-centered Lamb–Oseen vortex with $\Gamma = 21\ \mathrm{m}^2/\mathrm{s}$ and $r_c \sim 50$ mm [15].

rotor rotational speeds, this means that the downward speed of the wake vortices is on the order $V_C \sim 10$ m/s; as shown in the following, the motion of the wake vortices limits the maximum camera shutter time that can be used in the measurements in order to prevent motion-induced smearing of the aero-optical effects.

B. Optical Considerations

During synthetic wave-front measurements, such as depicted in Fig. 1, the camera is focused on the helicopter-mounted LED array in order to accurately resolve the positions of individual LEDs in the array. This means that aberrating flows passing between the array and the camera will be out of focus, so that the measured LED apparent displacements will be a spatially averaged effect of the aberrating flow; a diagram illustrating this optical effect is shown in Fig. 5. From geometrical considerations (see Fig. 5), the size of the spatial-averaging region is approximately

$$d_s = D_L\left(\frac{L_1}{L_1 + L_2}\right) < r_c \tag{5}$$

As shown in Fig. 4, most of the spatial effect of the vortex occurs within approximately five core radii of the vortex centerline. As such, in order to resolve the vortex's aero-optical effect, the spatial-averaging region should be approximately less than the vortex core radius; this condition is included in Eq. (5).

Referring to Eq. (5), although the distance L_1 is approximately equal to the blade radius R, the spatial-averaging region can conceivably be minimized by using a large L_2 or a small lens diameter D_L; however, both of these design choices adversely impact the measurement in other ways. Specifically, by geometric-optics principles, the size of the LED images on the camera CCD (charge-coupled device) array is

$$D_{t,\mathrm{CCD}} = D_t \frac{f_L}{(L_1 + L_2)} \tag{6}$$

whereas the apparent displacement of the LEDs on the camera CCD is

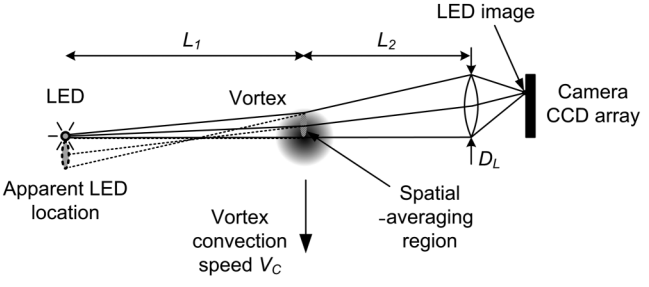

Fig. 5 Spatial averaging of vortex aero-optical effect due to optical setup.

$$d_t \approx \theta R \frac{f_L}{(L_1 + L_2)} \tag{7}$$

Equations (6) and (7) show that the LED image size and displacements on the CCD array are both increased by minimizing L_2, both of which improve the accuracy of the centroiding and wave-front calculations (see the following). Furthermore, the camera image brightness scales as $\sim D_L^2$, so that using a small D_L will also degrade the image quality by reducing image brightness. This point is particularly important if it is recognized that the optically active tip vortices are also moving past the camera at a convection speed V_C, so that the camera shutter time t_s must also be short enough that the results are not influenced by motion-induced smearing of the images:

$$V_C t_s \ll r_c \tag{8}$$

Equation (8) therefore shows that t_s cannot be increased without limit in order to improve the image brightness. In summary, the experiment optical design is a compromise between the competing requirements of Eqs. (5–8).

C. Optical Array

Given the requirements to use a small camera aperture and fast shutter speed, a critical component of the experiment design was to use optical targets with high brightness to improve the signal strength of the measurements. For this purpose, 3 W white LEDs were used, which also had a narrow 20 deg output cone of increased brightness for improved light emission toward the camera. To facilitate measurements from any angle without the need to reorient the optical target array, 3000 of the LEDs were mounted at 12.7 mm spacing onto a 0.4-m-diameter spherical acrylic ball. Mounting brackets were installed to attach the globe to the bottom of the helicopter fuselage, as shown in Fig. 1. A schematic of the "LED ball" optical array is shown in Fig. 6.

D. Experiment Parameters

The experimental configuration was designed based on the discussion in the preceding sections. The minimum safe distance from the camera to the helicopter was set at $L_1 + L_2 \sim 30$ m. A telephoto lens with $f_L = 1000$ mm and $D_L = 50$ mm was chosen, giving a spatial-averaging region of $d_s \sim 13$ mm, which was approximately one-fourth of the estimated vortex core radius of $r_c = 50$ mm. Using the telephoto lens, the camera field of regard at the location of the LED ball was ~0.7 m, which was enough to capture the full LED ball. The size of the high-speed camera CCD array was 25.4 mm with a pixel resolution of 1280×800. These CCD parameters gave maximum LED image displacements, computed using Eq. (7), of 0.17 pixels on the CCD array; the effect of this magnitude of dot displacement on measurement accuracy is discussed in the following section. Finally, the high-speed camera used for the measurements had a minimum camera exposure time of 0.1 ms, giving an image displacement $V_C t_s$ of approximately 1 mm, which was much smaller than the vortex size; see Eq. (8).

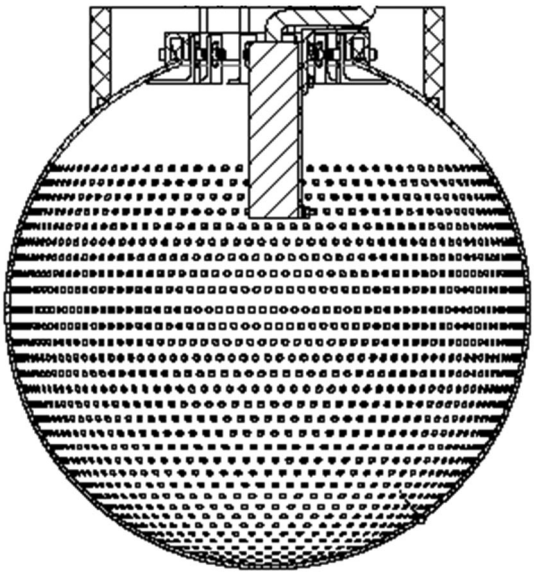

Fig. 6 Schematic of LED ball.

Due to the spherical curvature of the ball, it was found that only the LEDs in an approximately 0.2 m diameter circle centered on the LED ball could be clearly discerned from the camera images. From a geometric-optics analysis, this 0.2 m measurement range gave an effective size of the measurement aperture at the location of the rotor wake of $D_{AP} \sim 0.15$ m. This aperture size is plotted in Fig. 4 and shows that, although some of the aberration was filtered by the effective aperture boundaries, most of the optical effect of the vortex was adequately captured using the optical setup.

E. Uncertainty of Computed Wave Fronts

As shown in Sec. III, results for the synthetic wave-front approach were computed using postprocessing routines that were identical in most respects to routines that are used for standard Shack–Hartman measurements. The uncertainty of these postprocessing routines depends largely on how accurately the apparent displacements of the dots in each subaperture (or, in this case, the LED targets) can be determined from the camera images. An analysis of spot centroiding routines for use in Shack–Hartman wave-front calculations [23] showed that the centroiding error depends upon the spot size, the mean noise level (ratio of the average image background noise to the maximum image brightness), the signal-to-noise ratio (SNR), and the spot deflection amplitude. For the optical setup used for the measurements, the full-width half-maximum of the LED images on the camera CCD array was approximately 3 to 4 pixels, the mean image noise level was ~1%, and the SNR was approximately 40. For these parameters, average spot centroiding errors of approximately 0.05 pixels (95% confidence) were expected for simple first-moment centroiding routines [23], or roughly 30% of the maximum expected spot deflection of 0.17 pixels given previously.

Wave-front uncertainties can conceivably be computed from the spot deflection errors via an error-propagation analysis of the wave-front-calculation algorithm. However, as shown in [12–14], the aero-optical effect of the rotor wake is largely negligible except for the periods of time when a rotor vortex is actually passing through the field of regard of the optical system, and particularly when the vortex is centered in the optical aperture. From an aero-optical standpoint, the most important situation is therefore the aperture-centered case, shown in Fig. 4. A simple evaluation of the effect of spot deflection errors on wave-front uncertainty was therefore performed by computing the maximum possible wave-front error for the aperture-centered vortex. In this case, the maximum wave-front error occurs at the peak wave-front depression ($y = 0$ in Fig. 4) when all slope errors on either side of the peak combine additively. An analysis of this case for the optical setup employed gave a maximum wave-front error of approximately ± 0.27 μm, or around 35% of the predicted peak-to-valley OPD within the aperture boundaries shown in Fig. 4.

It should be noted that the preceding uncertainty estimate is a worst-case prediction and only applies to the magnitude of the wave fronts measured using the synthetic-wave-front approach. The temporal uncertainty of the data is related solely to the frame rate of the CCD camera, which is accurate to within less than 2 μs, which is effectively negligible based on the temporal resolution of the measurements. In summary, the experimental data can be expected to accurately show the temporal character of the aero-optical effect of the helicopter, as well as to show with reasonable accuracy the aero-optical effect of rotor–vortex passing events, which are the most important part of the overall optical effect of the helicopter. As such, the experimental results provide a useful validation of the current understanding of helicopter aero-optics, as well as providing valuable data for existing and future modeling efforts [24].

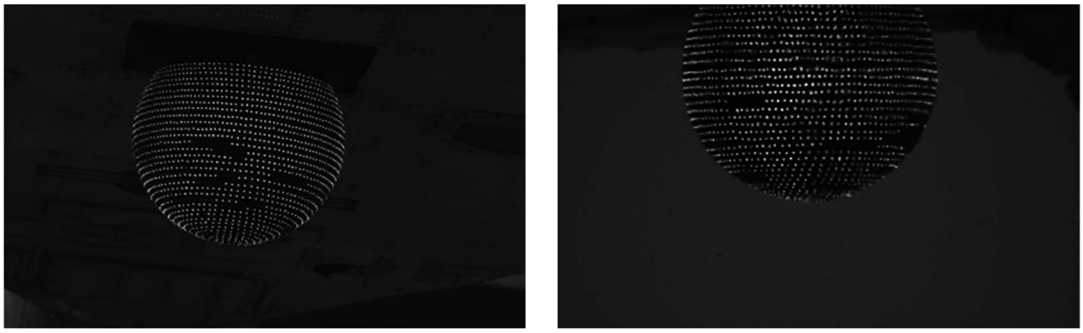

Fig. 7 Images of LED ball through rotor wake (left) and engine exhaust (right) of a helicopter in hover.

III. Experiment and Results

The experimental measurements were performed on a medium-sized four-bladed helicopter in hover. To reduce the influence of ground effect on the helicopter rotor wake, the helicopter above-ground height during the tests was approximately 16 m. The high-speed camera was mounted in an observation tower slightly below the height of the helicopter to ensure good visibility of the LED target array at any helicopter orientation. Ambient wind during the tests was negligible.

The measurements were made primarily with the camera viewing the helicopter from the side, although data viewing the helicopter from the rear through the exhaust plume of the helicopter engines were also acquired. For all measurements, the frame rate of the high-speed camera was 7.5 kHz with an exposure time of $t_s = 0.1$ ms and a frame resolution of 1280×800 pixels. Around 5000 to 7000 frames of data were acquired in a typical test. Examples of images viewing the LED ball from the helicopter side (through the rotor wake) and rear (through the engine exhaust) are shown in Fig. 7; the apparent displacement of individual LEDs by the aero-optical effect of the engine exhaust can be clearly seen in the right image of Fig. 7. Note that the dark patches in Fig. 7 were produced by a small number of LEDs that were not working at the time of the measurements.

A. Centroiding and Removal of Solid-Body Motion

First-moment centroids of the LEDs visible in each image were computed using

$$\boldsymbol{x} = \frac{\int I_p \boldsymbol{x}_p \, \mathrm{d}A}{\int I_p \, \mathrm{d}A} \tag{9}$$

where the integrations in Eq. (9) were performed over the local region surrounding each LED. Before computing the LED centroids, a noise threshold was also applied to each image, in which pixels that had an intensity of 15% or less of the maximum were eliminated from the centroiding calculations. All of the centroid positions were converted into coordinates in the physical plane of the LED ball by scaling the images based on the 0.4 m diameter of the LED ball.

The centroid data were next used to compute the solid-body motion of the LED ball. Solid-body motion is caused by motion or rotation of the helicopter, or by vibration of the camera itself, and therefore must be removed before calculation of optical data. In general, solid-body motion of the LED ball can be decomposed into three translations and three rotations with respect to the camera, shown in Fig. 8. However, since the optical analysis was performed using only the small region of the LED ball directly facing the camera, the primary effect of the rotations Ω_Y and Ω_Z on the measurement region of the ball was to produce additional effective translations T_Y and T_Z. As such, in practice, the rotations Ω_Y and Ω_Z were essentially fully removed by removal of the translations T_Y and T_Z, and were therefore not computed.

Time histories of the solid-body motions T_X, T_Y, and T_Z, and the rotation Ω_X for an example dataset acquired by viewing the helicopter from the side are shown in Fig. 9. As shown in the following, the wave-front analysis involved the calculations of the LED displacements from their "reference" locations, which were determined from the ensemble average of a block of camera images. Figure 10 shows the ensemble average of a representative set of camera images with and without the prior removal of solid-body motion, and clearly illustrates the need for this step of the analysis. The physical LED-ball motions shown in Fig. 9 can also provide additional insight into the vibration environment of the helicopter that could supplement accelerometer measurements.

B. Calculation of Wave-Front Distortions

Time-resolved wave-front distortions through the rotor wake were computed for a simulated beam with a 0.2 m aperture centered on the LED ball. The wave-front calculations followed the same procedure used for Shack–Hartman wave-front calculations, except that the LED positions were used instead of focused spot positions from a lenslet array.

The apparent motion of each LED in the aperture of the simulated beam was first computed as the difference in the position of the LED from its reference position:

$$\Delta \boldsymbol{x} = \boldsymbol{x} - \boldsymbol{x}_{\mathrm{ref}} \tag{10}$$

In Eq. (10), the reference position of each LED $\boldsymbol{x}_{\mathrm{ref}}$ was computed as the average position of the LED over the 1000 camera frames preceding and following the frame under analysis. Horizontal and vertical wave-front slopes were next computed using

$$\boldsymbol{s} = \frac{\Delta \boldsymbol{x}}{L_1} \tag{11}$$

In Eq. (11), L_1 is the distance from the LED ball to the location of the aero-optical flow causing the apparent displacement $\Delta \boldsymbol{x}$. For the rotor vortices, L_1 is the distance from the LED ball to the helicopter rotor vortices, or approximately the blade radius R. Wave fronts were

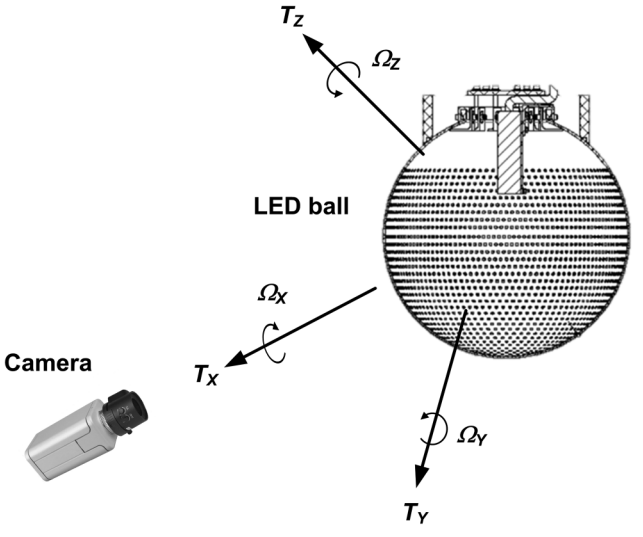

Fig. 8 General solid-body motions with respect to camera.

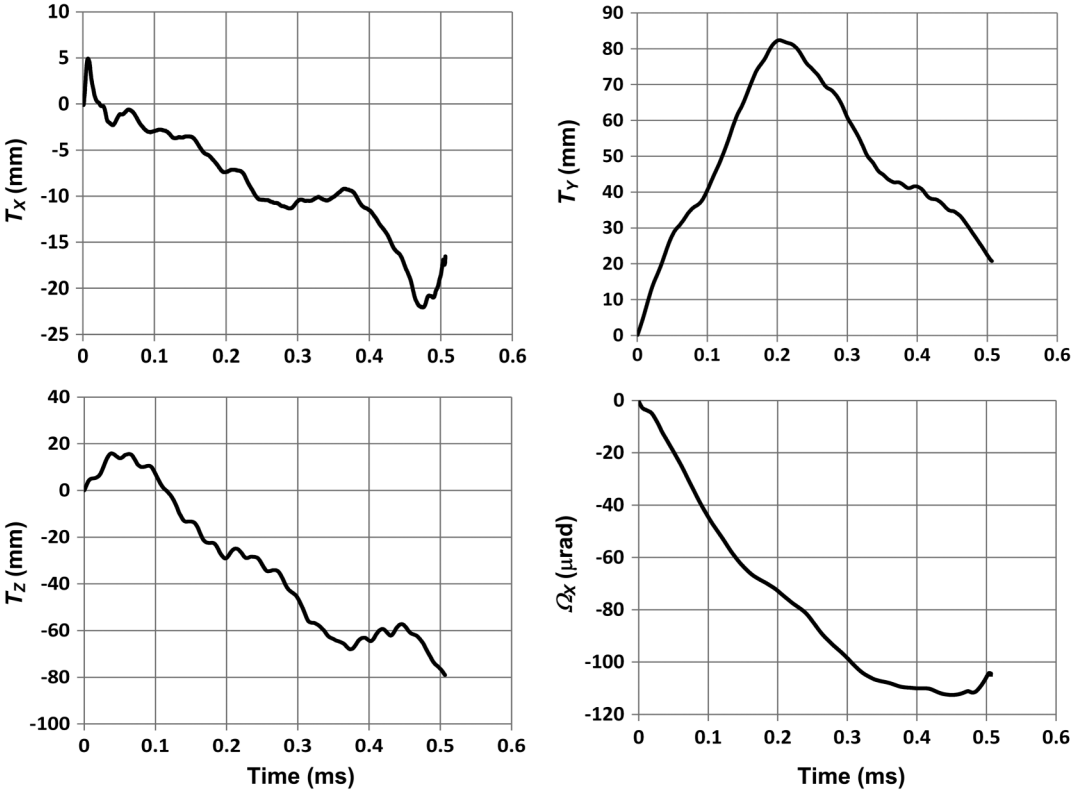

Fig. 9 Solid-body motions for a typical dataset.

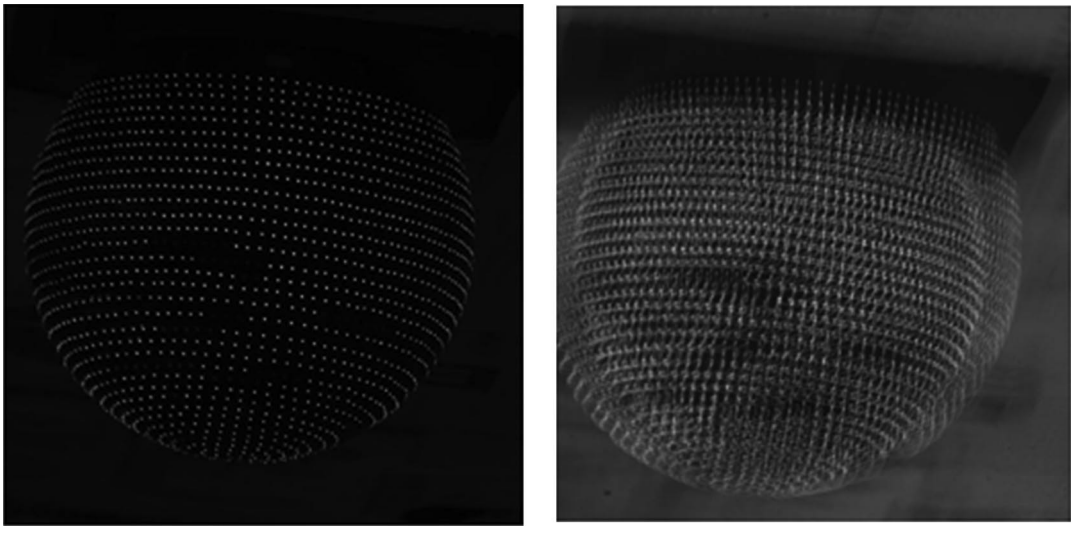

Fig. 10 Average of 2000 images of LED ball with (left) and without (right) prior removal of solid-body motions.

also computed for camera images acquired through the helicopter exhaust; for these cases, L_1 in Eq. (11) is the distance from the LED ball to the approximate location of the engine exhaust. Using the local slopes from Eq. (11) and the mean locations of the LEDs determined from the camera images, wave fronts were computed using the Southwell wave-front-reconstruction algorithm [25].

An example of a sequence of OPD distributions measured through the rotor wake is shown in Fig. 11. The OPDs in Fig. 11 have optical tip, tilt, and piston removed. The data clearly show a region of reduced OPD caused by the passage of a rotor vortex through the measurement aperture from top to bottom. Far-field irradiance patterns corresponding to the OPD distributions in Fig. 11 are plotted in Fig. 12, where the irradiance is shown nondimensionalized by the diffraction-limited peak irradiance I_0. The far-field patterns show the irradiance distributions if the beam were focused on a distant target, and were computed using Fourier-optics methods [26] for a nominal wavelength of 1 μm. To better show the behavior of the far-field patterns, Fig. 12 also shows circles that denote the first zero of the Airy disk for the aperture. The vertical tilt history over the time span of Fig. 11 is also shown in Fig. 13, with the times corresponding to the four frames in Fig. 11 denoted in Fig. 13. As noted previously, the magnitudes of both the OPD and optical tilt data have been influenced by the effective size of the aperture used in the measurements (see Fig. 4), and the data in Figs. 11–13 are shown with no adjustment for aperture effects.

The overall trend of the far-field irradiance patterns and optical tilt history shown in Figs. 12 and 13 corresponds to previous observations of the effect of the rotor wake described in [12–15]. Specifically, when there is no vortex in the simulated beam, the far-field pattern is close to its diffraction-limited distribution. As the vortex nears the beam, the vortex imposes primarily a tilt aberration in a direction normal to the vortex axis that causes an off-target shift of

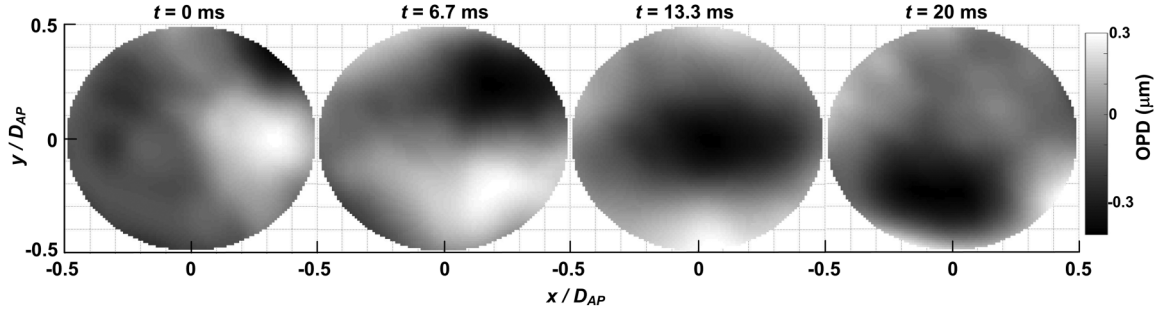

Fig. 11 Example of a sequence of OPD distributions measured through the helicopter rotor wake.

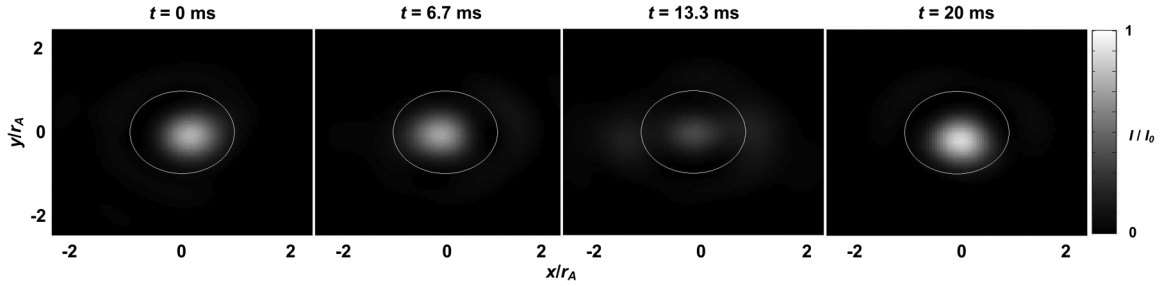

Fig. 12 Far-field irradiance patterns corresponding to OPD distributions shown in Fig. 11.

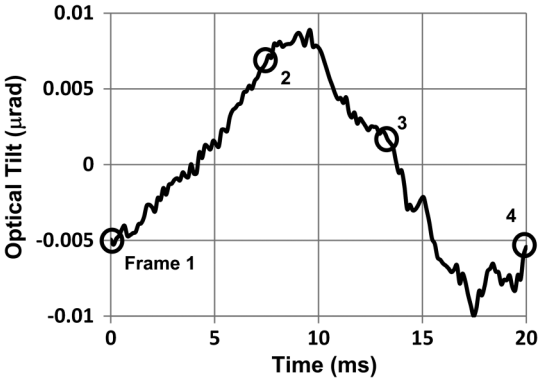

Fig. 13 Optical tilt history corresponding to the OPD sequence shown in Fig. 11, with the four frames in Fig. 11 denoted.

the beam, which is still otherwise well focused. Finally, the most substantial far-field effect occurs when the vortex is centered in the beam ($t = 13.3$ ms in Figs. 11 and 12), which causes substantial breakup and diffusion of the far-field pattern.

A time history of the Strehl ratio *St* for a dataset measured through the vortex wake of the helicopter is shown in Fig. 14. All *St* data were determined from direct calculations of the far-field irradiance patterns because, as shown in [27], the spatially localized nature of the vortex aberration means that methods of estimating *St* like the Maréchal approximation are inaccurate. The figure shows that the *St* through the rotor wake is reasonably large on average, with intermittent dips that correspond to the passage of a vortex through the simulated beam. The magnitude of the *St* dropouts, shown in Fig. 14, matches reasonably well the predictions made using prescribed-wake methods described in [12,14]; however, note that the exact effect of the rotor wake is sensitive to atmospheric and other conditions that might affect the diffusion of individual vortices after they are shed from the helicopter rotor blades.

Figure 14 also shows a Strehl history for a dataset measured through the helicopter exhaust. As expected, the large aero-optical effect of the exhaust, which is visible even to the naked eye, would make it impossible to focus an outgoing beam through the exhaust onto a far-field target. Without using some kind of correction methodology, the extent of the helicopter exhaust would therefore represent an obscuration in the effective field of regard of the optical system.

C. Spectral Content

Figure 14 shows that the *St* dropouts caused by the rotor wake occur at roughly the blade-passing frequency, which is an expected result since the largest magnitude optical aberrations occur whenever

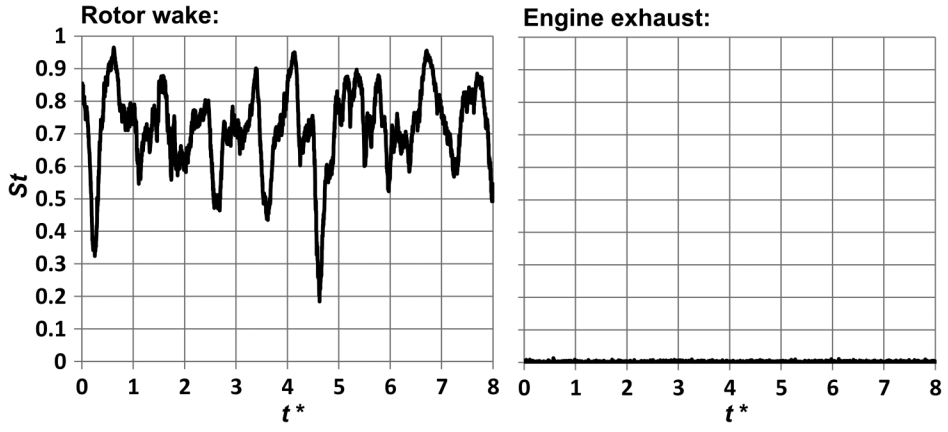

Fig. 14 Strehl ratio histories measured through rotor wake and engine exhaust.

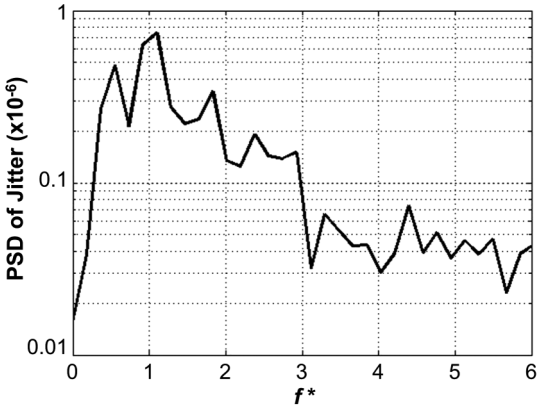

Fig. 15 Power spectral density (PSD) of optical jitter signal measured through rotor wake.

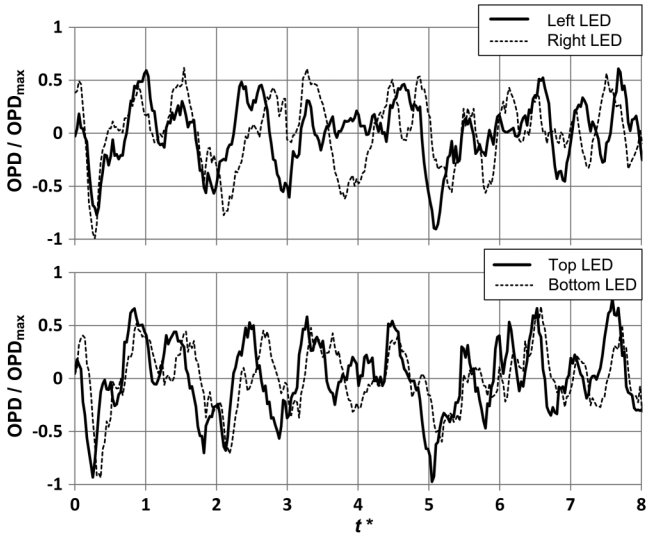

Fig. 16 OPD histories for two LEDs spaced horizontally by 0.2 m (top), and two LEDs spaced vertically by 0.2 m (bottom) on the LED ball.

a rotor vortex is centered in the aperture of the simulated beam. The *St* history in Fig. 14 also shows considerable variation in the magnitude and precise time separation between *St* dropouts, which is presumably caused by aperiodic effects such as vortex coupling, interaction, and wander. This variation in the passing frequency of the rotor vortices is also apparent in Fig. 15, which shows a power spectrum of the OPD slope, or "optical jitter," of a point near the center of the simulated aperture. In addition to a broadening of the peak around the blade-passing frequency, the spectrum in Fig. 15 also shows the existence of harmonics and subharmonics, and generally gives considerably more information on the detailed frequency content of the rotor wake than the prescribed-wake simulations of [12–14].

D. Optical Structure Motion

To conclude this section, the results of an analysis are shown that demonstrate the speed and direction of the dominant optical aberrations detected by the measurements. Figure 16 shows the measured OPDs at two LED locations separated by small horizontal and vertical distances on the LED ball. As shown in the figure, the OPDs of the horizontally separated LEDs show very little similarity, whereas the OPDs of the two vertically separated LEDs are nearly identical, except for a constant time offset. This result shows that the same optical aberration is moving past the lower LED at a slightly later time than the top LED, as expected for rotor vortices convecting downward past the LED ball. Cross-correlation functions for a typical point in time are also shown in Fig. 17, where the shifting peak for the vertically separated LEDs clearly shows the convection of an optical aberration downward past the LED ball. Cross correlations between the two vertically separated signals in Fig. 16 give a vertical convection velocity of approximately 9.6 m/s, which is close to the predicted convection speed of the helicopter rotor wake determined in Sec. II.

IV. Conclusions

Data on the aero-optical effect of a full-scale helicopter in flight have been acquired by tracking the motion of LEDs in a target array mounted beneath the helicopter fuselage. As shown by an analysis of the experimental uncertainty, the approach is capable of accurately resolving rotor–vortex passing events, as well as the temporal character of the optical aberrations, so that the resulting data constitute a useful addition to the current understanding of helicopter aero-optics.

The magnitude of the aero-optical effect of the rotor wake measured in the flight-test experiments is consistent with prescribed-wake analyses given in [12–15]; however, the flight-test data provide considerably more information on the frequency content of the rotor-wake aberrations, including spectral broadening and the presence of (sub)harmonics of the blade-passing frequency. The effort provides valuable information on the design and application of the synthetic wave-front approach for measurement of aero-optical data in a flight-test environment. The resulting flight-test data are also useful for beam-control studies and the validation of advanced modeling and simulation efforts.

Acknowledgments

These efforts were sponsored by the U.S. Office of Naval Research under award number N00014-12-1-0341. The U.S. Government is authorized to reproduce and distribute reprints for governmental purposes notwithstanding any copyright notation thereon.

References

[1] Gordeyev, S., Smith, A. E., Cress, J. A., and Jumper, E. J., "Experimental Studies of Aero-Optical Properties of Subsonic Turbulent Boundary Layers," *Journal of Fluid Mechanics*, Vol. 740, Feb. 2014, pp. 214–253.

[2] Wang, K., and Wang, M., "Aero-Optics of Subsonic Turbulent Boundary Layers," *Journal of Fluid Mechanics*, Vol. 696, April 2012, pp. 122–151.

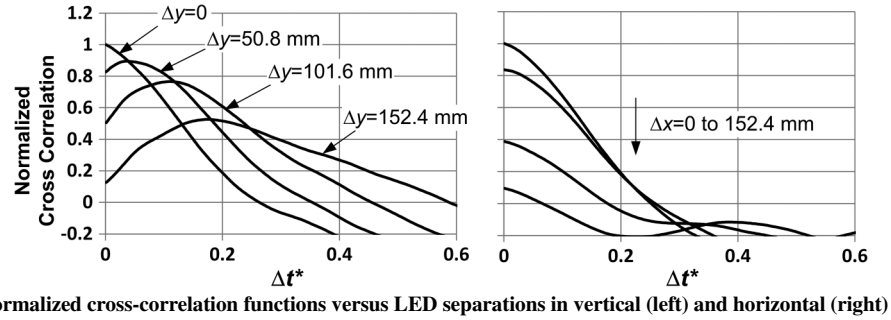

Fig. 17 Normalized cross-correlation functions versus LED separations in vertical (left) and horizontal (right) directions.

[3] Smith, A. E., Gordeyev, S., and Jumper, E., "Recent Measurements of Aero-Optical Effects Caused by Subsonic Boundary Layers," *Optical Engineering*, Vol. 52, No. 7, 2013, Paper 071404.
[4] Fitzgerald, E. J., and Jumper, E. J., "The Optical Distortion Mechanism in a Nearly Incompressible Free Shear Layer," *Journal of Fluid Mechanics*, Vol. 512, Aug. 2004, pp. 153–189.
[5] Rennie, R. M., Duffin, D. A., and Jumper, E. J., "Characterization and Aero-Optic Correction of a Forced Two-Dimensional, Weakly-Compressible Subsonic Free Shear Layer," *AIAA Journal*, Vol. 46, No. 11, 2008, pp. 2787–2795.
[6] Jumper, E. J., Zenk, M., Gordeyev, S., Cavalieri, D., and Whiteley, M. R., "Airborne Aero-Optics Laboratory," *Optical Engineering*, Vol. 52, No. 7, 2013, Paper 071408.
[7] DeLucca, N., Gordeyev, S., and Jumper, E., "In-Flight Aero-Optics of Turrets," *Optical Engineering*, Vol. 52, No. 7, 2013, Paper 071405.
[8] Porter, C., Gordeyev, S., Zenk, M., and Jumper, E., "Flight Measurements of the Aero-Optical Environment around a Flat-Windowed Turret," *AIAA Journal*, Vol. 51, No. 6, June 2013, pp. 1394–1403.
[9] Devenport, W., Rife, M., Stergios, L., and Follin, G. J., "The Structure and Development of a Wing-Tip Vortex," *Journal of Fluid Mechanics*, Vol. 326, Nov. 1996, pp. 67–106.
[10] Ellenrieder, K. V., and Cantwell, B. J., "Self-Similar, Slightly Compressible, Free Vortices," *Journal of Fluid Mechanics*, Vol. 426, Jan. 2000, pp. 293–315.
[11] Leishman, J., *Principles of Helicopter Aerodynamics*, Cambridge Aerospace Series, Cambridge Univ. Press, New York, 2000, pp. 418–450.
[12] Porter, C., Rennie, R. M., and Jumper, E. J., "The Aero-Optical Environment of a Helicopter in Hover," AIAA Paper 2011-1328, 2011.
[13] Porter, C., Rennie, R. M., and Jumper, E. J., "The Aero-Optical Environment of a Helicopter in Forward Flight," AIAA Paper 2011-3283, 2011.
[14] Porter, C., Rennie, R. M., and Jumper, E. J., "Computation of the Aero-Optical Environment of a Helicopter Using Prescribed-Wake Methods," *AIAA Journal*, Vol. 53, No. 3, 2015, pp. 532–541.
[15] Porter, C., Rennie, R. M., and Jumper, E. J., "Aero-Optic Effects of a Wing Tip Vortex," *AIAA Journal*, Vol. 51, No. 7, 2013, pp. 1533–1541.
[16] Landgrebe, A. J., "An Analytical Method for Predicting Rotor Wake Geometry," *Journal of the American Helicopter Society*, Vol. 14, No. 4, 1969, pp. 20–32.
[17] Landgrebe, A. J., "The Wake Geometry of a Hovering Helicopter Rotor and Its Influence on Rotor Performance," *Journal of the American Helicopter Society*, Vol. 17, No. 4, 1972, pp. 3–15.
[18] Beddeos, T. J., "A Wake Model for High Resolution Airloads," *Proceedings of the 2nd International Conference on Basic Rotorcraft Research*, Univ. of Maryland, College Park, MD, 1985.
[19] Ananthan, S., and Leishman, J. G., "Role of Filament Strain in the Free-Vortex Modeling of Rotor Wakes," *Journal of the American Helicopter Society*, Vol. 49, No. 2, 2004, pp. 176–191.
[20] Ramasamy, M., and Leishman, J. G., "A Reynolds Number-Based Blade Tip Vortex Model," *Journal of the American Helicopter Society*, Vol. 52, No. 3, 2007, pp. 214–223.
[21] Ramasamy, M., and Leishman, J. G., "Interdependence of Diffusion and Straining of Helicopter Blade Tip Vortices," *Journal of Aircraft*, Vol. 41, No. 5, 2004, pp. 1014–1024.
[22] Dalziel, S. B., Hughes, G. O., and Sutherland, B. R., "Whole-Field Density Measurements by 'Synthetic Schlieren'," *Experiments in Fluids*, Vol. 28, No. 4, April 2000, pp. 322–335.
[23] Nightingale, A. M., and Gordeyev, S., "Shack–Hartmann Wavefront Sensor Image Analysis: A Comparison of Centroiding Methods and Image Processing Techniques," *Optical Engineering*, Vol. 52, No. 7, March 2013, Paper 071413.
[24] Kelly, R., Jemcov, A., Rennie, R. M., Wang, K., Wang, M., and Jumper, E. J., "Computation of the Aero-Optical Effect of a Helicopter Rotor Wake Using Unsteady RANS and LES," *53rd AIAA Aerospace Sciences Meeting*, AIAA Paper 2015-0678, Jan. 2015.
[25] Southwell, W. H., "Wave-Front Estimation from Wave-Front Slope Measurements," *Journal of the Optical Society of America*, Vol. 70, No. 8, 1980, pp. 998–1006.
[26] Klein, M. V., *Optics*, 3rd ed., Wiley, New York, 1986, pp. 293–310.
[27] Ross, T. S., "Limitations and Applicability of the Maréchal Approximation," *Applied Optics*, Vol. 48, No. 10, 2009, pp. 1812–1818. doi:10.1364/AO.48.001812

M. N. Glauser
Associate Editor